Journal of *Marine Science and Engineering*

MDPI

Article

Deep-Towed Array Geometry Inversion Based on an Improved Particle Swarm Optimization Algorithm

Xiaohu Luo [1], Kai Liu [1,2,3,4], Yanliang Pei [1,2,3,4,*], Chenguang Liu [1,2,3,4], Xishuang Li [1,2,3,4] and Yibao Xiao [1]

[1] Key Laboratory of Marine Geology and Metallogeny, First Institute of Oceanography, Ministry of Natural Resources, Qingdao 266061, China; luoxiaohu@fio.org.cn (X.L.); liuk@fio.org.cn (K.L.); lcg@fio.org.cn (C.L.); lxs@fio.org.cn (X.L.); xiaoyibao@fio.org.cn (Y.X.)
[2] Laboratory for Marine Geology, Laoshan Laboratory, Qingdao 266237, China
[3] Key Laboratory of Submarine Acoustic Investigation and Application of Qingdao (Preparatory), Qingdao 266061, China
[4] Key Laboratory of Deep Sea Mineral Resources Development, Shandong (Preparatory), Qingdao 266061, China
* Correspondence: peiyanliang@fio.org.cn

Abstract: When marine deep-towed multichannel seismic data are processed, the description of the receiving array geometry significantly impacts the quality of the imaging profile. Therefore, achieving a highly precise description of the receiving array geometry is very important for the fine imaging of such data. While basic particle swarm optimization (PSO) is known for its ease of implementation and efficiency, it often exhibits a low convergence accuracy. Consequently, the PSO algorithm is improved by modifying the inertia weight and incorporating Gaussian mutation. In combination with the actual motion of the towing streamer during surveys, a strategy for inheriting particle positions is introduced. When each seismic shot is solved sequentially, the results from the previous shot can serve as the initial particle positions for the next shot. The results indicate that this strategy achieves superior fitness values and outperforms the basic PSO algorithm. This method exhibits simplicity, rapid optimization, and a favorable solution quality, thereby offering a valuable approach to deep-towed array geometry inversion. It enhances the efficiency of deep-towed seismic data processing and serves as a reference for similar applications.

Keywords: particle swarm optimization; array geometry inversion; near-bottom acoustic detection technology; deep-towed multichannel seismic system; algorithm improvement

Citation: Luo, X.; Liu, K.; Pei, Y.; Liu, C.; Li, X.; Xiao, Y. Deep-Towed Array Geometry Inversion Based on an Improved Particle Swarm Optimization Algorithm. *J. Mar. Sci. Eng.* **2024**, *12*, 282. https://doi.org/10.3390/jmse12020282

Academic Editor: Michael Lazar

Received: 19 December 2023
Revised: 30 January 2024
Accepted: 31 January 2024
Published: 4 February 2024

1. Introduction

Deep-towed multichannel seismic systems involve placing a seismic source and receivers at a certain height above the seabed and conducting seismic surveys in near-seabed environments [1,2]. These systems offer higher lateral and vertical resolution, increased signal-to-noise (SNR) ratios, and the ability to finely characterize the seafloor strata, making them powerful tools for marine gas hydrate exploration and underwater geological hazard assessment [3–5]. During surveys, seismic signals are generated from the source within the towing body, penetrating the seafloor under deep water and returning to the source. The signals are then received by the towed streamer trailing from the towing body, enabling high-resolution raw data to be acquired. The ultra-high-resolution attributes of deep-towed seismic technology necessitate the precise positioning of the seismic source and the hydrophone array within the towed streamer [6]. Thus, the description of the array geometry significantly influences the quality of the stacked profiles.

The Deep-Towed Acoustics and Geophysics System (DTAGS), developed by the U.S. Naval Research Laboratory (NRL) in the 1980s, was the first deep-towed seismic system capable of surveying at a thousand-meter depth. The geometry of deep-towed arrays was first described to calculate the positions of hydrophones between DTAGS

engineering nodes using linear interpolation [7]. Subsequently, Walia and Hannay [8] constrained the array geometry by incorporating the travel time of the sea surface reflection, thereby improving the accuracy of the relative positions of the sources and hydrophones within individual shot ensembles. Building on this work, He et al. [9] further constrained the array geometry by incorporating the travel time of the direct wave and jointly optimizing it with the travel time of the sea surface reflection. They introduced genetic algorithms to seek a global optimal solution, further optimizing the DTAGS array configuration. Following a similar approach, Kong and He [10] expanded the constraints by adding two optimization parameters: the average seawater seismic wave velocity at individual shot points and system errors in the engineering node depth. They used a genetic algorithm to further optimize the DTAGS array configuration, enhancing its overall performance.

The Kuiyang-ST2000 [2] was the first high-resolution deep-towed multichannel seismic system in China (Figure 1). It primarily consists of a towing body, towing streamer, and vessel connection streamer, using a plasma source with a maximum energy of 3000 J, a 48-channel digital seismic streamer (the channel spacing is 3.125 m), and an operating depth of 2000 m. It operates at a certain height, approximately 100 m, above the seabed [11]. In the context of array geometry inversion for the Kuiyang-ST2000 deep-towed seismic system, Li et al. [12] applied PSO to constrain the travel times of direct waves and seafloor-reflected waves, obtaining satisfactory horizontal stacked profiles. However, in practical computations, basic PSO exhibits a low convergence accuracy.

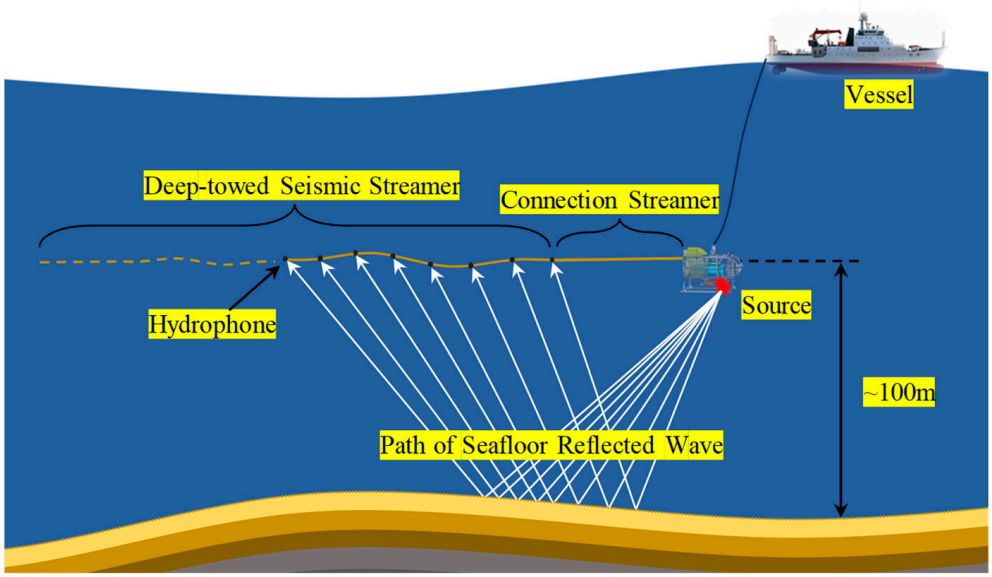

Figure 1. Kuiyang-ST2000 deep-towed multichannel seismic system.

Metaheuristic algorithms and other mathematical methods are applied to solve complex problems in different applications, such as thermal conductivity [13], seismic behavior [14], predictive models for seismic source parameters [15], spatial data mining [16], tunnel engineering [17], modeling for tsunami waves [18], the simulation of seismic wave propagation [19], and adaptive filtering for cooperative localization [20]. Array geometry inversion is a single-objective optimization problem that seeks the optimal solution under specific constraints. Due to the high dimensionality of the objective function in array geometry inversion, the algorithm's performance can be affected by the curse of dimensionality [21]. Therefore, algorithms must be improved to enhance the computational efficiency and achieve better results for the specified problem. Building on the research conducted by [12], this study is focused on improving the PSO using particle initialization strategies, inertia weight [22], and the addition of Gaussian mutation [23,24]. These improvements aim to enhance the algorithm's performance without increasing its complexity.

2. Establishment of Model

The Kuiyang-ST2000 deep-towed seismic system is equipped with a depth transducer and altimeter mounted onto the towing body. The altimeter records the source height, while the depth transducer records the source depth. After the data are smoothed with spline fitting, interpolation is performed at 0.2 m intervals, discretizing the seafloor interface depth.

In this study, the real travel time records of direct waves and seafloor-reflected waves from 100 consecutive shots are examined, and the seafloor interface in the designated interval is discretized. Since seismic signals are generally reflected from the seafloor behind the source, for each excitation, the lateral distance before the source is set to 75 m, and the lateral distance behind the source is set to 150 m as the probable interval where the seafloor reflection point could be located (Figure 2). After discretization, there are a total of 1125 discrete points per shot, and due to multiple overlaps, there is a cumulative total of 4250 discrete points for the 100 shots.

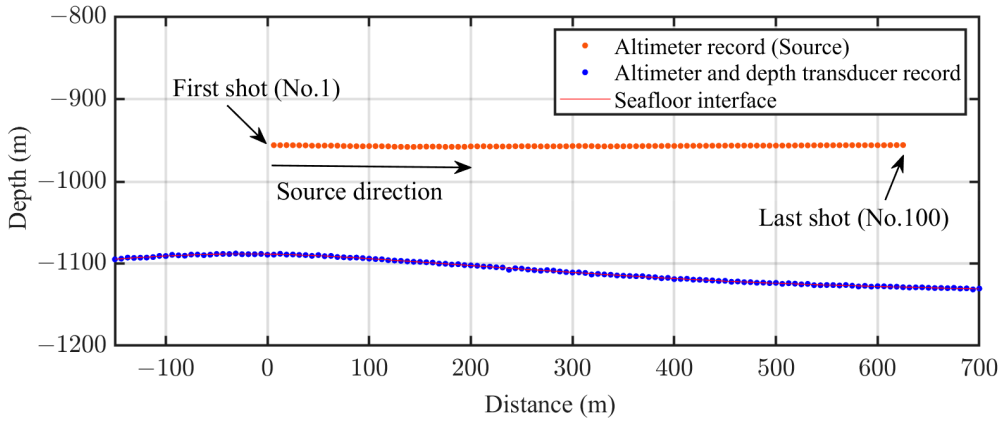

Figure 2. The relative location of the source and seafloor interface.

3. Streamer Array Geometry Inversion Using an Improved PSO Algorithm

3.1. Basic Particle Swarm Optimization (PSO) Algorithm

PSO is a metaheuristic algorithm that generates a swarm of particles P within a specific search space [25]. Each particle moves through the search space based on its current position and velocity, updating its position at each iteration using predefined formulas. By leveraging the collective experiences of individuals and the group, PSO aims to discover the optimal fitness value within the given search space.

The variables and formulas for the update process of the particle positions and velocities in the PSO algorithm are defined as follows: D denotes the dimensionality of the search space, and n denotes the number of particles in each search space. For particle i:

(1) Position: $\overline{P}_i = (p_{i1}, p_{i2}, \ldots, p_{iD})^T$;

(2) Velocity: $\overline{V}_i = (v_{i1}, v_{i2}, \ldots, v_{iD})^T$;

(3) Individual best position: $\overline{P}_{bi} = (p_{i1}, p_{i2}, \ldots, p_{iD})^T$;

(4) Global best position: $\overline{P}_G = (p_{i1}, p_{i2}, \ldots, p_{iD})^T$.

During the iterations, the update formulas for the particle velocities and positions are as follows:

$$V_{id}^{k+1} = \omega V_{id}^{k} + c_1 r_1 \left(P_{bid}^{k} - P_{id}^{k}\right) + c_2 r_2 \left(P_{Gid}^{k} - P_{id}^{k}\right) \quad (1)$$

$$P_{id}^{k+1} = P_{id}^{k} + V_{id}^{k+1} \quad (2)$$

where ω represents the inertia weight. c_1 is the personal learning factor. c_2 is the global learning factor. r_1 and r_2 are random numbers within the range [0, 1]. V_{id}^{k} and P_{id}^{k} denote the velocity vector and position vector of particle i in dimension d at iteration k. P_{bid}^{k} and P_{Gid}^{k} are the individual best position and global best position experienced by particle i in dimension d at iteration k.

The experimental data were collected from a real scene and contained a lot of noise; therefore, they could not be directly used for the model training. The primary task of data noise removal is to remove incomplete or wrong data. Here, the data cleaning was divided into the removal of outliers and missing values. Data points significantly far away from the fitted curve were marked as outliers using a regression fit between the sound speed and each physical parameter. The missing sound speed values and physical parameters of each sample were simultaneously removed to improve the data quality and integrity.

3.2. Improved Inversion Strategy Based on the PSO Algorithm

3.2.1. Improved PSO Algorithm

In a specific problem, the optimization parameter settings are crucial for tuning the algorithm's performance. When basic PSO is used to optimize the objective function discussed in Section 3.1, issues such as slow convergence and low precision can occur. We often use more iterations to increase the iteration accuracy, which consumes more time.

This issue is often attributed to the inertia weight ω in the PSO algorithm. In the early stages of iterations, ω is set relatively high to enhance the global search capabilities. As the iterations progress, ω is gradually reduced to boost the local search capabilities. Typically, ω falls within the range of 0 to 1.

To address this issue, we employ a nonlinear decreasing function to adjust the inertia weight, causing it to gradually decrease as the number of iterations increases. This is expressed as:

$$\omega = (1 - a)^t \tag{3}$$

where t represents the current iteration number and a is the inertia weight decay factor, which influences how rapidly the inertia weight decreases as the number of iterations progresses.

Furthermore, in the basic PSO algorithm, the particle motion is guided by local and global best solutions. However, when a solution near the local best is not the global best, the particles may stagnate. The Gaussian mutation strategy can help the particles overcome this stagnation, making them more likely to explore nearby solutions. Therefore, Formula (2) can be enhanced as follows:

$$P_{id}^{k+1} = P_{id}^{k} + V_{id}^{k+1} + Gaussian\left(0, \sigma^2\right) \tag{4}$$

where $Gaussian\left(0, \sigma^2\right)$ represents a random number following a Gaussian distribution with a mean of 0 and a variance of σ^2. We also employ a nonlinear decreasing function to set the variance (σ^2) for the Gaussian mutation. This approach gradually reduces the strength of the perturbation in the Gaussian mutation. This is expressed as:

$$\sigma^2 = h(1 - b)^t \tag{5}$$

where t represents the current iteration number, h is the perturbation strength adjustment factor, and b is the variance decay factor, which is used to ensure that the variance is relatively large in the early iterations and gradually decreases in the later iterations.

Dynamically adjusting the variance in the Gaussian mutation strategy helps control the exploration and exploitation trade-off in the optimization process.

3.2.2. Objective Function and Methods

During the survey, a uniform trigger strategy is employed for seismic source excitation, with a spacing interval (X) of 6.25 m. The lateral and vertical distances (c_x, c_y) between the seismic source and the connection streamer are 2 m and 0.6 m, respectively, and the length of the connection streamer is 12.5 m.

Due to the relatively low and stable vessel speed and modest water current during the survey, which result in a minimal streamer feather angle, and considering only the vertical motion of the seismic source and streamer in a two-dimensional space, we can set a point on the sea surface as the origin of the coordinates. For consecutive shots, the coordinates

of the source can be represented as (nX, H_n), where n denotes the number of shots and H_n denotes the depth of the seismic source for shot n. The hydrophone interval (w) is 3.125 m and the pitch angle of the hydrophone positions is denoted by θ. As the connection streamer is not composed of rigid material, to maintain stability in the inversion results and achieve a smoother array geometry, considering the positions of three virtual channels for the connection streamer is sufficient. In this scenario, for shot n, the coordinates of the first hydrophone (including the three virtual channels) can be represented as $\left(R^n_{x1}, R^n_{y1}\right)$, where:

$$R^n_{x1} = nX + c_x + wcos\theta_1 \tag{6}$$

$$R^n_{y1} = H_n - c_y + wsin\theta_1 \tag{7}$$

The coordinates of hydrophone k (including the three virtual channels) can be represented as $\left(R^n_{xk}, R^n_{yk}\right)$, where:

$$R^n_{xk} = R^n_{xk-1} + wcos\theta_k \tag{8}$$

$$R^n_{yk} = R^n_{yk-1} + wsin\theta_k \tag{9}$$

In this model, θ_k represents the pitch angle of hydrophone k. The values of k, ranging from 1 to 3, correspond to the virtual channels introduced to achieve smoother array geometry in the inversion. The values of k from 4 to 51 correspond to the 48 real seismic channels.

The travel times of the direct wave (T_{pickD}) and seafloor-reflected wave (T_{pickF}) are obtained by manually picking from actual seismic records. During the inversion process, the minimum propagation time method is used to calculate the propagation distance based on the discretized seafloor interface mentioned earlier. The depths of the seafloor surface and source in each shot are illustrated in Figure 2, and the position of the hydrophones can be preliminarily set according to the position of the source and Formulas (6)–(9). The propagation times T_{calD} and T_{calF} are calculated from the relative position of the hydrophones and the seafloor surface. Setting the sound velocity (v) of the seawater as 1485 m/s, the following objective function is established:

$$o = argmin\left(\sum_1^{48}\left(T_{pickD} - T_{calD}\right)^2 + \sum_1^{48}\left(T_{pickF} - T_{calF}\right)^2\right) \tag{10}$$

In the objective function, T_{calD} denotes the calculated travel times for the direct wave, and T_{calF} denotes the calculated travel times for the seafloor-reflected wave obtained by traversing the seafloor interface using the shortest path algorithm.

The objective function is aimed at minimizing the discrepancy between the calculated travel times and the record travel times (T_{pickD} and T_{pickF}) by adjusting the array geometry parameters to obtain the best fit.

When a string of deep-towed seismic array geometries is being evaluated, PSO should be called at each shot. As the time span or shot frequency of the deep-towed seismic surveys increases, the number of shots and their corresponding array geometry calculations also increase, leading to a higher computation time and higher costs.

To address this, an improved strategy that combines the characteristics of seismic surveys and the physical properties of streamer movement is proposed. During a continuous near-seabed deep-towed survey, the vessel's velocity remains relatively stable, and the time intervals between source triggers are short. Without external factors such as streamer deployment and retrieval affecting the streamer, the streamer attitude should not abruptly change during consecutive excitations. Thus, the array geometry at a given source excitation can serve as a reference and guide for the array geometry in the next excitation. In the context of PSO, this corresponds to initializing the particle positions. Consequently, a strategy is introduced in which the array geometry from the previous shot ensemble is inherited to initialize the particle positions.

Compared to basic PSO for continuous array geometry inversion, the strategy for generating particle initializations is improved and combined with the characteristics of a seismic survey in this paper. Additionally, the PSO algorithm is improved by modifying the

inertia weight and introducing the Gaussian mutation strategy. These enhancements are designed to make the algorithm more suitable for deep-towed array geometry inversion. A flowchart of the proposed improvement strategy is depicted in Figure 3. The dashed boxes in Figure 3 provide a relatively clear method of improvement.

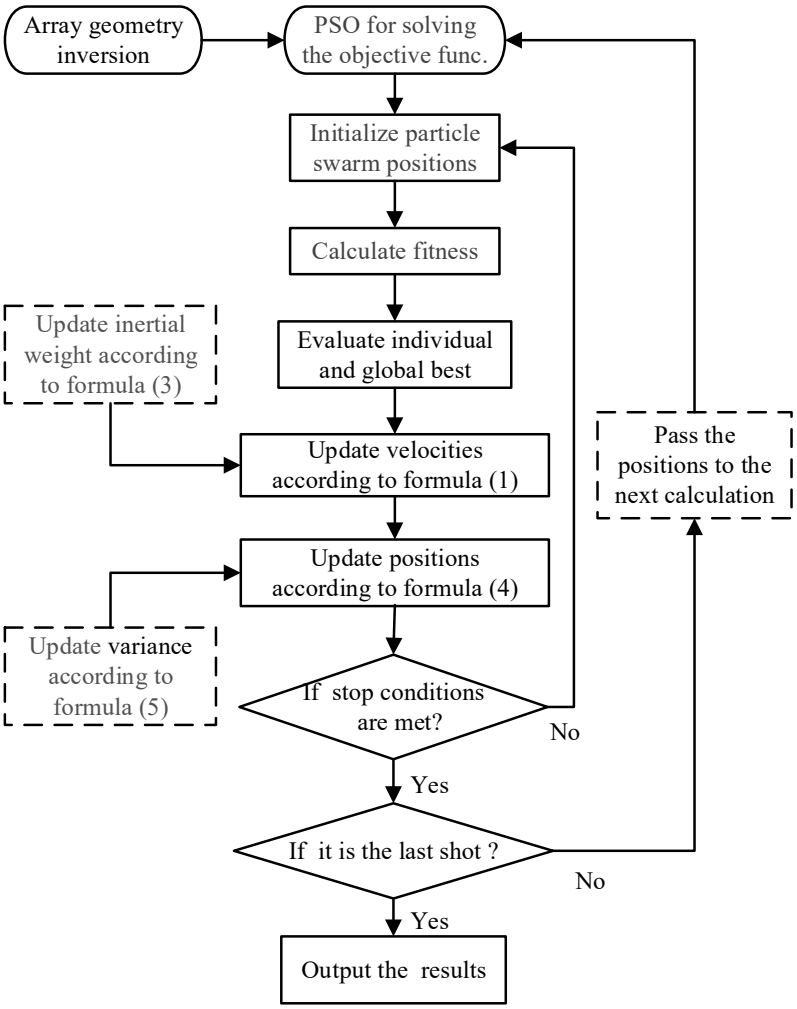

Figure 3. Flowchart of array geometry inversion based on improved PSO in this study.

4. Results

4.1. Comparative Analysis of Practical Data Inversion Using Different Strategies

In this section, the results of array geometry inversion using four different strategies are compared. These strategies are as follows:

Strategy 1: Basic PSO (PSO)

Strategy 2: PSO with the improvements described in Section 3.2.1 (PSO-G)

Strategy 3: PSO with particle initialization using inherited positions (PSO-C)

Strategy 4: PSO combining strategy 2 and strategy 3 (PSO-CG)

The content in Section 3 illustrates that the objective function has a dimension of 51. To facilitate the comparison of the efficiency and accuracy of different algorithms, the following settings are applied:

Strategies 1 and 2: Initialize all particle positions to zero.

Strategies 3 and 4: Initialize the particle positions to the results from the previous calculation.

Strategies 1 and 3: Set ω to 1.

Strategies 2 and 4: Set ω to the value obtained when a is 0.01 in Formula (3) and set σ^2 to the value obtained when h is 0.005 and b is 0.05 in Formula (5).

All four strategies use 100 particles and a maximum iteration count of 100, and the learning factors c_1 and c_2 are set to 1 for all strategies. These settings enable a standardized comparison of the efficiencies and accuracies of the four different strategies.

Additionally, since no particle position calculation results from previous shots exist for the initial calculation, PSO-G is applied to the receiving array geometry inversion using the arrival time records from the first shot. This process yields a convergence position in 51 dimensions. To ensure accuracy, this position is recalculated once. The resulting 51-dimensional particle position data are then used as the initial particle position for the second calculation in both strategy 2 and strategy 4.

The fitness curves for the second shot after applying different strategies are obtained and depicted in Figure 4. Strategy 1 and strategy 2 use an initialization of all-zero particle positions, resulting in an initial objective function value of approximately 850. The final convergence values for these strategies are 74.9142 and 5.5361, respectively.

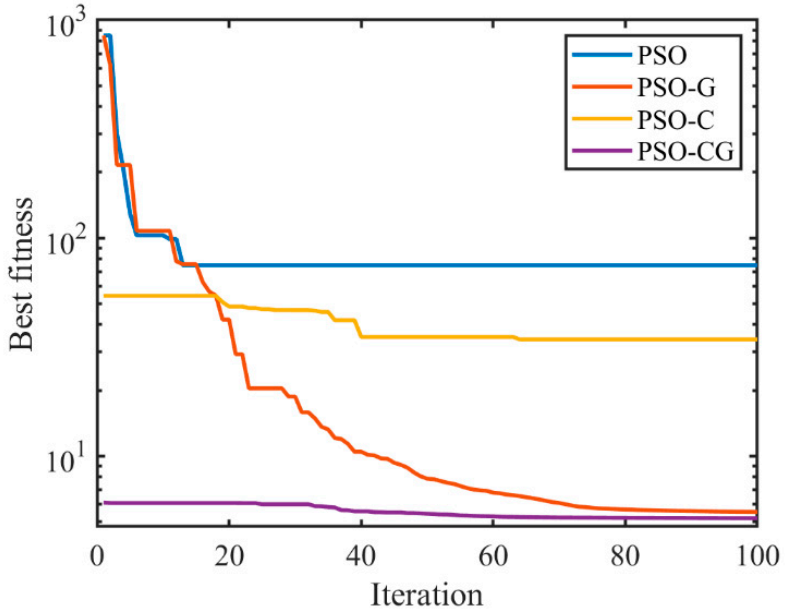

Figure 4. Fitness curves using different strategies.

The significant difference in the convergence values after iteration indicates that applying the improved PSO can effectively mitigate the convergence to local optima, thereby enhancing the inversion precision.

Strategy 3 and strategy 4 utilize the particle positions from the previous calculation as the initial positions for the current calculation. Consequently, at the beginning of the evaluation, the objective function values are 54.2851 and 6.1057. The final convergence values for these strategies are 34.2585 and 5.1771, respectively. Strategy 3 does not converge much in this instance due to the limited precision of the basic particle swarm algorithm. The convergence curve for strategy 4 demonstrates that the proposed improved particle swarm algorithm can effectively improve the calculation accuracy.

Taking the results of the 10 continuous calculations for the 21st to 30th shots as an example (Figure 5), when the termination conditions are the same, the basic particle swarm algorithm exhibits poor array geometry smoothness and converges to a local optimum. This is due to the differing particle velocity and position update strategies set in later iterations.

Strategy 1 employs a fixed inertia weight value, which hinders the algorithm's effectiveness in later iterations, preventing the array geometry from being precisely described.

Strategy 2, an improvement of PSO, yields better results.

Strategy 3 inherits the array geometry results from the previous shot ensemble. Since this result is near the strongest result of basic PSO, the array geometries for 10 consecutive shots are similar for these two strategies.

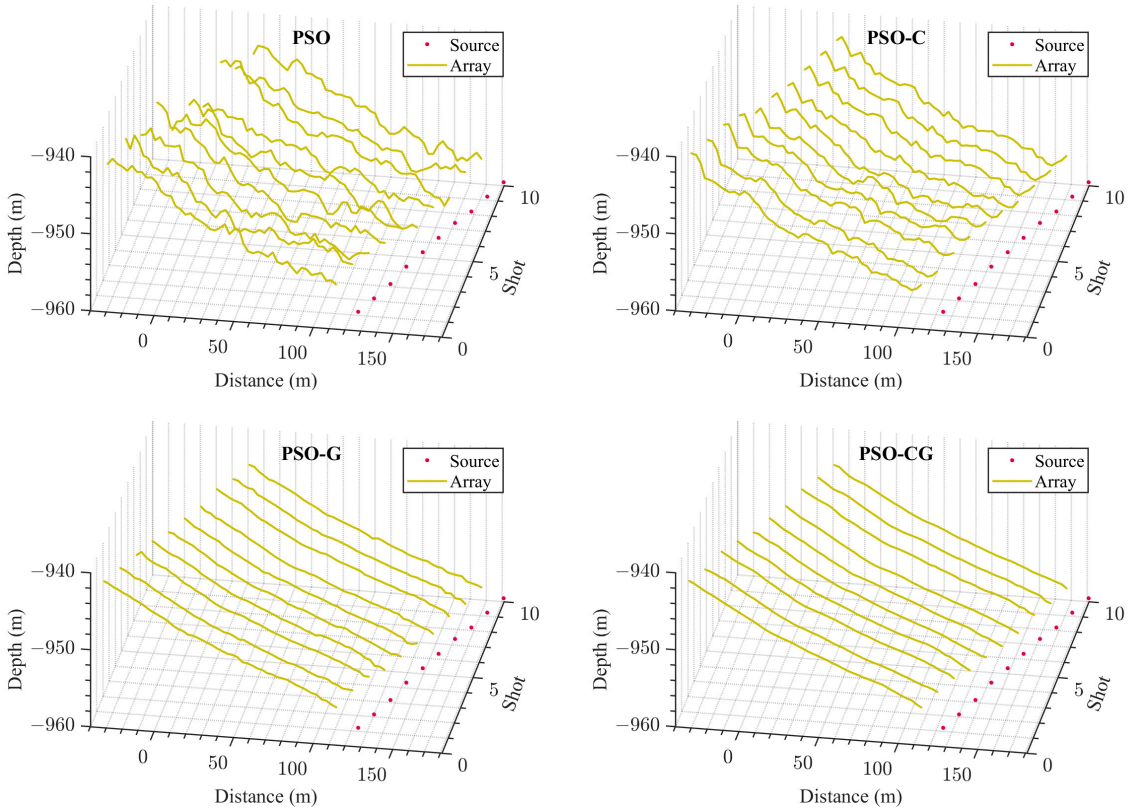

Figure 5. Calculated array geometry using different strategies (Strategy 1: upper left; strategy 2: lower left; strategy 3: upper right; strategy 4: lower right).

In contrast, strategy 4, which incorporates enhancements, yields a smoother array geometry. The roll angles between shots indicate continuous changes, which align more closely with the actual streamer's motion attitude.

To reduce errors, calculations are performed for the 100 shots, and the average results are obtained. The results are presented in Table 1, where "zeros (1,51)" represents a 1×51 vector filled with zeros, and "last (1,51)" indicates the results from the previous shot. The findings reveal that the objective function under strategy 4 (PSO-CG) achieves the highest convergence accuracy.

Table 1. Fitness performance: applying different strategies for inversion.

Strategy	Maximum Iteration	Initialization of Particle Vector	Inertia Weight Generation Strategy	Average Best Fitness Value
1. PSO	100	zeros (1,51)	1	57.963654
2. PSO-G	100	zeros (1,51)	Formula (3)	4.514059
3. PSO-C	100	last (1,51)	1	23.299226
4. PSO-CG	100	last (1,51)	Formula (3)	4.126673

4.2. Analysis of the Results before and after Improvement

The improved array geometry inversion, which was obtained using the proposed method, is incorporated into the seismic data headers. Subsequently, a floating datum is applied for static correction and velocity analysis using Geovation software from CGG Company, France, resulting in the creation of velocity spectra and common midpoint (CMP) gathers.

Figure 6 displays the velocity spectra and the corresponding 430th CMP gather for the array geometries estimated using strategy 1 and strategy 4. The estimations obtained using the proposed approach better focus on the velocity spectra than those obtained using the other strategies.

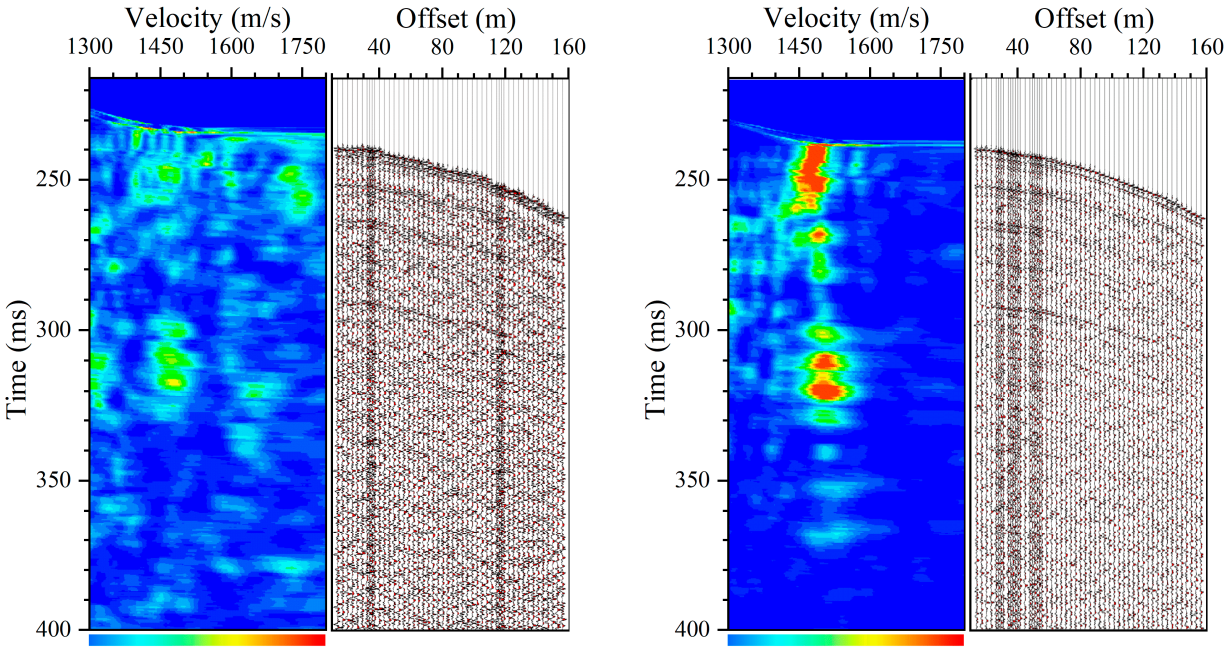

Figure 6. Velocity spectrum and corresponding CMP gather (**left**: strategy 1 (PSO); **right**: strategy 4 (PSO-CG)).

Figure 7 illustrates the stack profiles of the streamer attitudes estimated using strategy 1 and strategy 4. The stack profiles generated using strategy 4 demonstrate a higher precision and resolution than those generated using strategy 1. These improved stack profiles effectively reveal the subsurface geological structures.

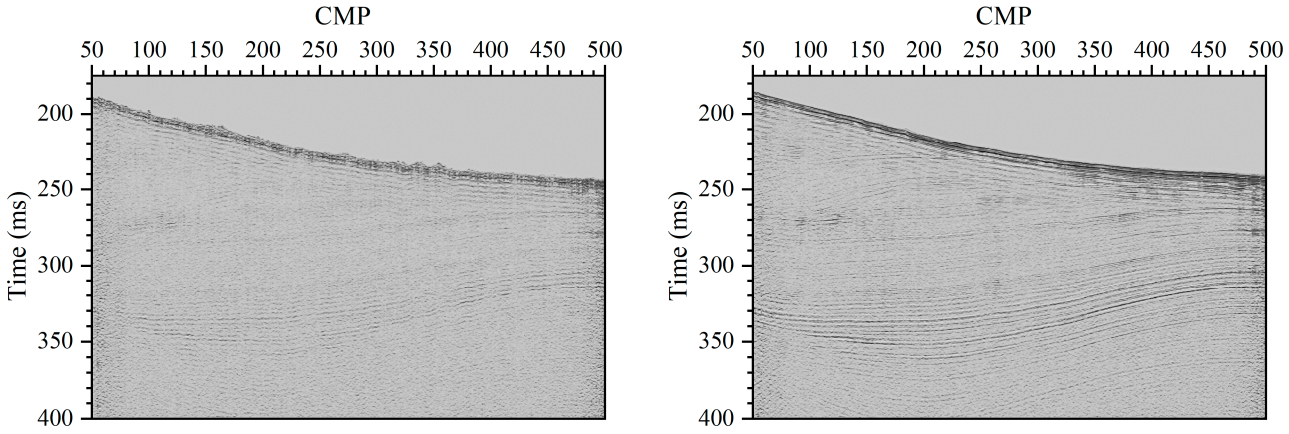

Figure 7. Comparison of stacked profiles before and after improvement (**left**: strategy 1 (PSO); **right**: strategy 4 (PSO-CG)).

In summary, the results indicate that the proposed strategy, strategy 4, enhances the focus of the velocity spectra and yields a higher level of detail and resolution in the stack profiles, thus exhibiting a stronger ability to reveal subsurface geological structures than strategy 1.

4.3. Performances of Different Strategies Excluding Error Effects

Due to the combined impact of errors, such as the manual picking errors in the first break, data-fitting errors, and the initial errors in the near-bottom underwater sound velocity, the optimal fitness is not equal to 0. Therefore, to eliminate the influence of errors on the algorithm's convergence, the results of 100 consecutive calculations using strategy 4 are assumed to represent the real array geometries. Under these geometries, the

travel times of the direct wave T_{mD} and seafloor reflection wave T_{mF} for each shot are calculated using the shortest path algorithm instead of the previously described T_{pickD} and T_{pickF}. All other settings are kept the same, and the objective function can now be expressed as:

$$o = argmin\left(\sum_1^{48}(T_{mD} - T_{calD})^2 + \sum_1^{48}(T_{mF} - T_{calF})^2\right) \quad (11)$$

After applying the four strategies from Section 3.1 again, we obtain the average best-fitness-value-calculated positioning error of 100 shots (Figure 8).

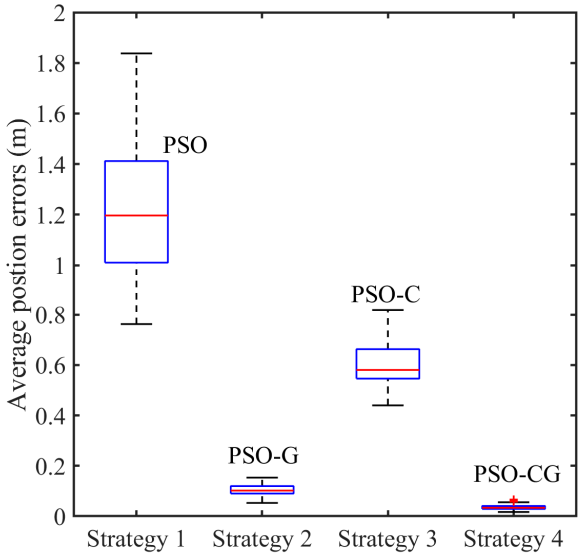

Figure 8. Average hydrophone positioning errors in 100 shots.

Figure 8 depicts the error distributions of the performances of the four strategies. Hydrophone positioning errors, which average 100 shots and 48 hydrophone positions in each shot, are calculated based on the coordinate difference. In this way, the interference of errors is eliminated. In theory, the optimal values of the best fitness value and position error should be zeroes, while the actual values are as Figure 8 and Table 2 show.

Table 2. Performance and positioning errors using different strategies.

Strategy	Maximum Iteration	Initialization of Particle Vector	Inertia Weight Generation Strategy	Average Time Cost (s)	Average Best Fitness Value	Position Error (m) (Per Hydrophone)
1. PSO	100	zeros (1,51)	1	2.41898	38.97512	1.21158
2. PSO-G	100	zeros (1,51)	Formula (3)	2.43994	0.32962	0.10353
3. PSO-C	100	last (1,51)	1	2.59914	9.38700	0.59843
4. PSO-CG	100	last (1,51)	Formula (3)	2.48249	0.04001	0.03528

Strategies 1 and 2 did not apply inherited particle positions as initial positions, and strategies 1 and 3 did not use the improved PSO algorithm; although these strategies have moderate spreads, with no outliers detected, their errors are higher than those in strategy 4. Meanwhile, strategies 3 and 4 applied inherited particle positions as the initial positions, and the boxes for them appear to be significantly skewed to the left, with few outliers detected in strategy 4. Using the improved PSO algorithm when applying strategy 4 yields minimal errors, which shows its robustness as well.

We averaged each hydrophone position error from each shot, and the results of using strategy 4 are depicted. Each hydrophone positioning error is 0.03528 m, while strategy 1 (1.21158 m), strategy 2 (0.10353 m), and strategy 3 (0.59843 m) all exhibit higher errors. These results are presented in Table 2. Additionally, the average time cost shows that the supposed strategy did not have a significant impact on the time consumption.

The calculation results, excluding the influence of errors, indicate that employing the improved inversion strategy based on the proposed approach can accelerate the convergence while ensuring a sufficiently high level of accuracy.

5. Conclusions

In this study, an improved deep-towed seismic array geometry estimation method based on an improved PSO algorithm is introduced. The method improves the algorithm by modifying the inertia weight generation strategy, introducing a Gaussian mutation mechanism, and considering the specific motion characteristics of deep-towed seismic streamers. Under the same number of iterations, PSO-CG shows a better convergence accuracy. The average best fitness achieved is 0.04001, while its time cost does not significantly increase. Although the position errors are small, more refined settings for the parameters and combining this approach with other methods can further reduce the errors. It will more precisely describe the array geometry, significantly improving the resolution and signal-to-noise ratio of deep-towed multichannel seismic imaging profiles.

This paper is primarily focused on array geometry inversion from the perspective of direct arrival times and seafloor reflection arrival times. Manually picking the travel time of direct waves and seafloor reflection waves can introduce errors, and the initial assumption of the near-seabed water sound velocity affects the computed results. Future research will investigate methods for automatically picking the travel time of direct waves and seafloor reflection waves and optimizing the near-seabed water sound velocity assumptions to further enhance the model's accuracy.

Author Contributions: Conceptualization, X.L. (Xiaohu Luo); methodology, X.L. (Xiaohu Luo) and K.L.; software, X.L. (Xiaohu Luo), Y.X. and K.L.; validation, X.L. (Xiaohu Luo) and K.L.; formal analysis, X.L. (Xiaohu Luo); investigation, Y.P.; resources and data curation, C.L. and Y.P.; writing—original draft preparation, X.L. (Xiaohu Luo), K.L. and X.L. (Xishuang Li); writing—review and editing, Y.P., X.L. (Xiaohu Luo) and C.L.; visualization, Y.P. and X.L. (Xiaohu Luo); supervision, C.L. and Y.P. All authors have read and agreed to the published version of the manuscript.

Funding: The study was supported by the special funds of Laoshan Laboratory (no. LSKJ202203604) and the National Key Research and Development Program of China (no. 2023YFC2811200, no. 2016YFC0303901).

Institutional Review Board Statement: Not applicable.

Informed Consent Statement: Not applicable.

Data Availability Statement: The data presented in this study are available on request from the corresponding author.

Conflicts of Interest: The authors declare no conflicts of interest.

Nomenclature

Decision parameters

Symbol	Definition	Size	Value
D	Dimensionality of the search space	1×1	51
$\overline{P}_i$	Position vector of particle i	1×51	
$\overline{V}_i$	Velocity vector of particle i	1×51	
$\overline{P}_{bi}$	Personal best vector of particle i	1×51	
$\overline{P}_G$	Global best vector	1×51	
ω	Inertia weight	1×1	
c_1	Personal learning factor	1×1	1
c_2	Global learning factor	1×1	1
r_1, r_2	Random vectors within [0, 1]	1×1	
a	Inertia weight decay factor	1×1	0.01
b	Perturbation strength adjustment factor	1×1	0.05
h	Variance decay factor	1×1	0.005

Model parameters

Symbol	Definition	Size	Value	Unit
X	Excitation spacing interval	1×1	6.25	m
c_x	Lateral distance from source to streamer	1×1	2	m
c_y	Vertical distance from source to streamer	1×1	0.6	m
w	Hydrophone interval	1×1	3.125	m
H_n	Depth of source for shot n	1×1		m
θ_k	Pitch angle for hydrophone k	1×1		rad
R^n_{xk}	Abscissa for hydrophone k for shot n	1×1		m
R^n_{yk}	Ordinate for hydrophone k for shot n	1×1		m
v	Sound velocity of seawater	1×1	1485	m/s
T_{pickD}	Real travel time vector of direct wave	1×48		ms
T_{pickF}	Real travel time vector of seafloor-reflected wave	1×48		ms
T_{calD}	Calculated travel time vector for direct wave	1×48		ms
T_{calF}	Calculated travel time vector for seafloor-reflected wave	1×48		ms
T_{mD}	Model travel time vector of direct wave	1×48		ms
T_{mF}	Model travel time vector of seafloor-reflected wave	1×48		ms

References

1. Gettrust, J.F.; Grimm, M.; Madosik, S.; Rowe, M. Results of a deep-tow multichannel survey on the Bermuda Rise. *Geophys. Res. Lett.* **1988**, *15*, 1413–1416. [CrossRef]
2. Pei, Y.L.; Wen, M.M.; Liu, B.H.; Zhang, L.C.; Yu, K.B.; Wei, Z.R.; Zong, L.; Lian, Y.H.; Yan, K.P. Design and Implementation of Near Ocean Bottom High Resolution Multichannel Seismic System. *Adv. Mar. Sci.* **2022**, *40*, 79–89.
3. Talukder, A.R.; Bialas, J.; Klaeschen, D.; Buerk, D.; Brueckmann, W.; Reston, T.; Breitzke, M. High-resolution, deep tow, multichannel seismic and sidescan sonar survey of the submarine mounds and associated BSR off Nicaragua pacific margin. *Mar. Geol.* **2007**, *241*, 33–43. [CrossRef]
4. Riboulot, V.; Ker, S.; Sultan, N.; Thomas, Y.; Marsset, B.; Scalabrin, C.; Ruffine, L.; Boulart, C.; Ion, G. Freshwater lake to salt-water sea causing widespread hydrate dissociation in the Black Sea. *Nat. Commun.* **2018**, *9*, 117. [CrossRef] [PubMed]
5. Wei, J.G.; Liang, J.Q.; Lu, J.G.; Zhang, W.; He, Y.L. Characteristics and dynamics of gas hydrate systems in the northwestern South China Sea–Results of the fifth gas hydrate drilling expedition. *Mar. Pet. Geol.* **2019**, *110*, 287–298. [CrossRef]
6. Marsset, B.; Ker, S.; Thomas, Y.; Colin, F. Deep-towed high resolution seismic imaging II: Determination of P-wave velocity distribution. *Deep Sea Res. Part I Oceanogr. Res. Pap.* **2018**, *132*, 29–36. [CrossRef]
7. Rowe, M.M.; Gettrust, J.F. Fine structure of methane hydrate-bearing sediments on the Blake Outer Ridge as determined from deep-tow multichannel seismic data. *J. Geophys. Res. Solid Earth* **1993**, *98*, 463–473. [CrossRef]
8. Walia, R.; Hannay, D. Source and receiver geometry corrections for deep towed multichannel seismic data. *Geophys. Res. Lett.* **1999**, *26*, 1993–1996. [CrossRef]
9. He, T.; Spence, G.D.; Wood, W.T.; Riedel, M.; Hyndman, R.D. Imaging a hydrate-related cold vent offshore Vancouver Island from deep-towed multichannel seismic data. *Geophysics* **2009**, *74*, B23–B36. [CrossRef]
10. Kong, F.D.; He, T. Accurate Array Geometry Inversion of Deep-Towed Multichannel Seismic System. *Acta Sci. Nat. Univ. Pekin.* **2012**, *48*, 8. [CrossRef]
11. Li, Z.; Shahrajabian, H.; Bagherzadeh, S.A.; Jadidi, H.; Karimipour, A.; Tlili, I. Effects of nano-clay content, foaming temperature and foaming time on density and cell size of PVC matrix foam by presented Least Absolute Shrinkage and Selection Operator statistical regression via suitable experiments as a function of MMT content. *Phys. A Stat. Mech. Its Appl.* **2020**, *537*, 122637. [CrossRef]
12. Zhang, X.; Zhou, G.; Liu, X.; Fan, Y.; Meng, E.; Yang, J.; Huang, Y. Experimental and numerical analysis of seismic behaviour for recycled aggregate concrete filled circular steel tube frames. *Comput. Concr.* **2023**, *31*, 537.
13. Liu, Q.Y.; Li, D.Q.; Tang, X.S.; Du, W. Predictive models for seismic source parameters based on machine learning and general orthogonal regression approaches. *Bull. Seismol. Soc. Am.* **2023**, *113*, 2363–2376. [CrossRef]
14. Zhou, G.; Wang, Z.; Li, Q. Spatial negative co-location pattern directional mining algorithm with join-based prevalence. *Remote Sens.* **2022**, *14*, 2103. [CrossRef]
15. Hu, D.; Li, Y.; Yang, X.; Liang, X.; Zhang, K.; Liang, X. Experiment and Application of NATM Tunnel Deformation Monitoring Based on 3D Laser Scanning. *Struct. Control Health Monit.* **2023**, *2023*, 3341788. [CrossRef]
16. Dai, Z.; Li, X.; Lan, B. Three-Dimensional Modeling of Tsunami Waves Triggered by Submarine Landslides Based on the Smoothed Particle Hydrodynamics Method. *J. Mar. Sci. Eng.* **2023**, *11*, 2015. [CrossRef]
17. Wu, M.; Ba, Z.; Liang, J. A procedure for 3D simulation of seismic wave propagation considering source-path-site effects: Theory, verification and application. *Earthq. Eng. Struct. Dyn.* **2022**, *51*, 2925–2955. [CrossRef]
18. Xu, B.; Wang, X.; Zhang, J.; Guo, Y.; Razzaqi, A.A. A novel adaptive filtering for cooperative localization under compass failure and non-gaussian noise. *IEEE Trans. Veh. Technol.* **2022**, *71*, 3737–3749. [CrossRef]

19. Pei, Y.L.; Wen, M.M.; Wei, Z.R.; Liu, B.H.; Liu, K.; Kan, G.M. Data processing of the Kuiyang-ST2000 deep-towed high-resolution multichannel seismic system and application to South China Sea data. *J. Oceanol. Limnol.* **2023**, *41*, 644–659. [CrossRef]
20. Li, J.; Pei, Y.L.; Liu, C.G.; Zhang, L.W.; Luo, X.H.; Liu, K.; Li, W.L. A robust array geometry inversion method for a deep-towed multichannel seismic system with a complex seafloor. *Front. Mar. Sci.* **2023**, *10*, 1283061. [CrossRef]
21. Lalwani, S.; Sharma, H.; Satapathy, S.C.; Deep, K.; Bansal, J.C. A survey on parallel particle swarm optimization algorithms. *Arab. J. Sci. Eng.* **2019**, *44*, 2899–2923. [CrossRef]
22. Chatterjee, A.; Siarry, P. Nonlinear inertia weight variation for dynamic adaptation in particle swarm optimization. *Comput. Oper. Res.* **2006**, *33*, 859–871. [CrossRef]
23. Van den Bergh, F.; Engelbrecht, A.P. A new locally convergent particle swarm optimiser. In Proceedings of the IEEE International Conference on Systems, Man and Cybernetics, Yasmine Hammamet, Tunisia, 6–9 October 2002; p. 6.
24. Higashi, N.; Iba, H. Particle swarm optimization with Gaussian mutation. In Proceedings of the 2003 IEEE Swarm Intelligence Symposium, SIS'03 (Cat. No. 03EX706), Indianapolis, IN, USA, 26 April 2003; pp. 72–79.
25. Kennedy, J.; Eberhart, R. Particle swarm optimization. In Proceedings of the ICNN'95-International Conference on Neural Networks, Perth, Australia, 27 November–1 December 1995; pp. 1942–1948.